33rd Fluid Dynamics Conference
Orlando, Florida / June 23–26, 2003

**AIAA 2003-4162**

# EFFECT OF SUB-BOUNDARY LAYER VORTEX GENERATORS ON INCIDENT TURBULENCE

J. Casper*, J. C. Lin†, and C. S. Yao‡
NASA Langley Research Center
Hampton, Virginia

## Abstract

Sub-boundary layer vortex generators were tested in a wind tunnel to assess their effect on the velocity field within the wake region of a turbulent boundary layer. Both mean flow quantities and turbulence statistics were measured. Although very small relative to the boundary layer thickness, these so-called micro vortex generators were found to have a measurable effect on the power spectra and integral length scales of the turbulence at a distance many times the height of the devices themselves. In addition, the potential acoustic impact of these devices is also discussed. Measured turbulence spectra are used as input to an acoustic formulation in a manner that compares predicted sound pressure levels that result from the incident boundary-layer turbulence, with and without the vortex generators in the flow.

## Nomenclature

$b$ = airfoil semi-span (m)
$C$ = airfoil chord (m)
$c_0$ = ambient sound speed (m/s)
$f$ = frequency (Hz)
$E_{uu}$ = 1D streamwise spectrum ($m^3$/rad-$s^2$)
$E_{ww}$ = 1D transverse spectrum ($m^3$/rad-$s^2$)
$g$ = velocity-to-pressure transfer function
$h(k_c)$ = scaling function ( Eqs. (7) and (8) )
$k_c$ = $\omega / U_c$, convective wave number (rad/m)
$\Delta P$ = unsteady surface pressure jump (Pa)
$p$ = unsteady surface pressure (Pa)
$p'$ = radiated sound pressure radiated (Pa)
$r$ = distance from source to observer (m)
$t$ = observer time (s)
$U_c$ = local mean flow speed (m/s)
$U_\infty$ = freestream speed (m/s)
$u$ = streamwise turbulent velocity (m/s)
$\overline{u^2}$ = mean-square streamwise turbulence
$u_{rms}$ = $\left(\overline{u^2}\right)^{1/2}$
$w$ = transverse turbulent velocity (m/s)
$v$ = vertical turbulent velocity (m/s)
$\vec{x}$ = $[x_1, x_2, x_3]^T$, observer position
$\Phi_{ww}$ = 2D transverse spectrum ($m^4$/rad$^2$-$s^2$)
$\lambda$ = $c_0 / f$, acoustic wavelength (m)
$\rho_0$ = ambient density (kg/$m^3$)
$\tau$ = source time (s)
$\phi$ = random phase variable (radians)
$\omega$ = $2\pi f$, circular frequency (radians/s)

## 1. Introduction

Vortex generators (VGs), first introduced by Taylor [1], have long been used to control boundary-layer flows by redirecting the outer flow to the wall region via streamwise vortices [2, 3]. Such devices are also known to alter the boundary-layer turbulence downstream of the VGs [4]. The VGs used in those previous studies generally consisted of a row of small vanes with a device height approximately the size of the boundary-layer thickness $\delta$. The VGs were set at an angle of incidence to the local flow to produce an array of streamwise vortices. However, for some flow control applications, the use of these $\delta$-scale VGs could produce excess residual drag through conversion of a vehicle's forward momentum into unrecoverable turbulence in its wake.

---

* Research Scientist, Computational Modeling and Simulation Branch, AIAA Senior Member.
† Senior Research Scientist, Flow Modeling and Control Branch, AIAA Associate Fellow.
‡ Senior Research Scientist, Flow Modeling and Control Branch.

One method of reducing the device drag and improving the system efficiency is to generate an embedded streamwise vortex using minimal near-wall protuberances through substantially reduced device height. Lin et al. [5] showed that, with a reduced device height in the range of 10 to 20 percent of boundary layer thickness, these "micro" vortex generators (MVGs) could still provide sufficient momentum transfer to prevent boundary-layer separation. With proper design guidance, MVGs can efficiently produce streamwise vortices that prevent separation, yet do not dominate the boundary layer after the flow-control objective is achieved [6].

Sub-boundary-layer scale vortex generators have been successfully demonstrated in a variety of applications. For instance, such devices were shown to significantly increase the lift-to-drag ratio on multi-element high-lift airfoils [6, 7], or to effectively control separation in an adverse pressure gradient [8]. However, of even greater interest with respect to the present study are applications of sub-boundary layer vortex generators near the entrances and exits of inlet ducts to enhance the performance of jet engines, e.g. [9,10,11,12]. Such studies have led to an increased interest in obtaining information on the potential acoustic impact of these devices.

The experimental work reported here was designed to quantify the effect of MVGs on the unsteady velocity field within the wake region of a turbulent boundary layer. A second objective was to determine the impact that the flow-field alteration has on the acoustic field downstream of the MVGs. Thirdly, the authors wanted to determine whether an economical procedure could be developed for flow control design studies when acoustics play a roll in the design space.

The details of the experiment are described in the following section. A "nacelle-like" model is installed near the floor of a low-speed wind tunnel so that the entire model is immersed in a turbulent boundary layer. Mean flow and turbulence measurements are taken between the nacelle model and tunnel floor. MVGs are attached on the lower side of the nacelle model, near its leading edge, and the downstream flow field is again measured. Hot-wire anemometry is used to determine turbulence spectra which are in turn used to calculate velocity correlation functions and integral length scales. The flow field measurements, with and without MVGs, are reported and compared in Section 3.

Section 4 begins with a brief acoustic analysis for an airfoil in a turbulent stream. The objective of this section is to determine the downstream effect of the MVGs on the turbulence as it relates to the incidence of that turbulence on an airfoil, e.g., a stator beneath the nacelle model. Such a configuration could be viewed as a simplified model for the potential control of inlet distortion downstream of an engine inlet. The flow measurements, with and without MVGs, are used as inflow conditions in an acoustic analysis to determine a sound-pressure-level (SPL) differential. Concluding remarks are given in Section 5.

## 2. Experimental Apparatus

### 2.1. Facility, Test Set-up, and MVGs

The experimental measurements in this report were conducted in the NASA Langley Shear Flow Tunnel. This facility is a subsonic open-circuit wind tunnel with a 4.67-m long test section that is 50.80 cm by 71.12 cm (20 x 28 inches) in cross section. A 1.27-cm-thick splitter plate was mounted 10.16 cm above the original test section floor to bypass the converging section boundary layer to eliminate any upstream influence. The new boundary layer on the splitter plate was artificially tripped with a 5.08-cm-wide strip of sandpaper (36 grit) located 25.40 cm from the leading edge of the splitter plate.

A 40.64-cm-chord simulated nacelle model was installed parallel to the splitter plate with its leading edge located 3.2 m downstream of the boundary-layer trip to create a flow-through passage that spanned the width of the test section (71.12 cm). Schematics of the experimental set-up in the tunnel and the nacelle model are illustrated in Figs. 1(a) and 1(b), respectively. The model is manufactured in three chord-wise pieces: an aluminum leading edge, a center portion of constant thickness, and an aluminum trailing edge. The central portion was made of glass to provide transparency for particle-image velocimetry (PIV) measurements. However, it was decided that such measurements would not be necessary for the current study.

The nominal flow speed for all reported test runs is 35.05 m/sec (115 ft/sec). The turbulent boundary layer just upstream of the nacelle model is fully developed and has a thickness $\delta \approx 4.70$ cm. The approximate Reynolds numbers at this location, relative to distance downstream of the splitter plate edge and the boundary layer thickness are, respectively, $7.48\times10^{6}$ and $1.10\times10^{5}$. The flow-through passage has an initial opening gap of 3.23 cm at its leading edge and 3.30 cm at its trailing edge, as well as a constant gap of 2.67 cm under the model's central section where the flow is measured.

All data involving MVGs in this report were generated with delta-wing type MVGs, shown

schematically in Fig. 2. These devices have a vane height of 2.54 mm (Fig. 2). The MVGs were arranged in a row of counter-rotating pairs, at alternating incident angles of ±23 degrees, with the pairs spaced 1.27 cm apart (Fig. 2). The configuration was placed on the lower surface of the nacelle model within 3.81 cm of the leading edge. An underside view of the nacelle model with MVGs installed is shown in Fig. 3.

### 2.2. Instrumentation

A single component hot-wire anemometry system was used to measure the turbulence spectrum in a plane perpendicular to the mean flow within the flow-through passage. The hot-wire probe consisted of a platinum-plated tungsten wire 0.0005 cm in diameter with an un-plated active length of 0.13 cm and operated at an overheat ratio of 1.8. The probe was connected to a constant-temperature anemometer (DISA Type 55M01). The bridge output from the hot-wire anemometer was acquired by a PC computer through an eight-channel simultaneous sample, 16-bit analog-to-digital (A/D) converter (HP E1433A). The sampling rate of 66.67 kHz was used to obtain 100 data blocks, each consisting of 8192 readings. The signal input was low-pass filtered at 26 kHz and high-pass filtered at 3Hz.

A two-dimensional traverse system was used to control the hot-wire probe's motion from outside the test section through two spanwise slots, one on the tunnel ceiling and the other towards the trailing edge of the nacelle model. All hot-wire data were taken in a streamwise perpendicular plane located within the flow-through passage beneath the transparent section of the nacelle model (Fig. 1(b)). The coordinate system for these measurements is shown in Fig. 4. The coordinate origin is on the tunnel floor directly beneath the mid-span location of the nacelle model leading edge and the *x*-axis is located along the tunnel floor centerline $z = 0$. A $9 \times 9$ grid of survey points was selected within the plane $x$ = 19.05 cm for the flow field measurements. Nine vertical points above the splitter plate were chosen at $y$ = 1.02, 1.52, 1.78, 1.91, 2.03, 2.16, 2.29, 2.41, and 2.51 cm. Nine equally spaced spanwise points were selected in $-1.27 \le z \le 1.27$ cm. The upper extent of the data plane was limited to $y$ = 2.51 cm because of the physical dimension of the probe stem. The lower extent was truncated at $y$ = 1.02 cm because measurements below this height showed no significant effect from MVGs of the size considered here (see Section 3).

Immediately prior to and after each hot-wire survey, the hot-wire probe was moved to a fixed free-stream location above the nacelle model to be calibrated against a nearby pitot-static probe for free-stream velocities ranging from 3.05 to 36.58 m/sec. The anemometer bridge output and pitot-static free-stream velocity can be accurately related through a fourth-order polynomial curve [13]. The polynomial coefficients determined from each calibration were used to compute both the mean and fluctuating velocities from each respective hot-wire survey. The velocity results were then entered into a Fast Fourier Transform (FFT) subroutine that calculated the turbulence spectrum. In order to maintain the high resolution of the fluctuating velocities, mean and time-dependent signals were separated before the A/D conversion and combined for the total velocity (mean plus fluctuating) computation and separated again thereafter. As a further assurance of the hot-wire data accuracy, a temperature sensor on the ceiling of the tunnel entrance indicated that the variation in tunnel temperature for any survey was within 0.28 degree C. The measured velocity error of the current hot-wire system is estimated to be within ±2%, and the hot-wire position is accurate to within ±0.04 mm, similar to the hot-wire system reported by Pack and Seifert [14].

## 3. Flow Measurements

All measurements were performed at a nominal tunnel speed of 35.05 m/sec at each location on a 9-by-9-point grid within the flow-through passage as described in the previous section. Both mean flow values and turbulence statistics were measured in order to fully characterize the baseline flow and its alteration with the use of MVGs. Velocity correlation functions were calculated from measured turbulence spectra and in turn were used to compute integral length scales. A discussion of relevant flow measurements follows.

### 3.1. Mean Flow

Mean flow measurements, for the baseline flow and the flow with MVGs, were inspected at all 81 points within the data plane for spanwise homogeneity. The largest deviation from spanwise homogeneity was found to occur in the flow with MVGs, at the highest vertical station ($y$ = 2.51 cm) where the flow is most heavily influenced by the MVGs as well as by the additional boundary layer on the nacelle model underside. The magnitude of this velocity deviation was no more than one m/s, or less than three percent of the tunnel speed. Therefore, the discussion will focus on the vertical centerline of the data plane.

Fig. 5 shows measurements of the mean flow speed $U_c(y)$, at the nine vertical stations on the tunnel centerline ($z = 0$), for the baseline run and with MVGs installed, in order to visually compare the two mean flow states. Clearly, the MVGs have slowed the mean

flow speed as expected, because the MVGs on the underside of the nacelle model's leading edge have slightly increased the blockage at the passage entrance. The trend indicated in Fig. 5 is that the MVGs cause larger reductions in $U_c(y)$ as the measurement station approaches the nacelle model underside, with a maximum reduction of approximately one m/s.

### 3.2. Turbulence Statistics

Similar to the mean flow measurements, the turbulence measurements were found to deviate most from spanwise homogeneity at the vertical measurement station nearest the nacelle model underside, for the flow with MVGs. The size of the largest deviation in turbulence intensity was approximately 0.6 percent of the local mean flow speed.

Fig. 6 shows the local turbulence intensity at $z = 0$ for the baseline flow and the flow with MVGs. The local turbulence intensity $u_c'(y)$ is defined by

$$u_c'(y) = u_{\text{rms}} / U_c(y) \ , \quad u_{\text{rms}} = \left[ \overline{u^2}(y) \right]^{1/2}$$

where $\overline{u^2}(y)$ is the streamwise local mean-square turbulence. The MVGs have increased the local turbulence intensity levels in the upper half of the measurement plane and decreased the levels in the lower half. Perhaps the most interesting observation in Fig. 6 is the vertical distance over which the MVGs have affected the flow. Although the MVGs protrude only 2.54 mm from the nacelle model surface, their effect on the mean turbulence is measurable throughout the vertical extent of the data measurement plane, i.e., approximately 15 mm.

Figs. 7(a) – 7(d) show the power spectral density (PSD) of the streamwise turbulence at four of the nine vertical measurement stations along $z = 0$. The value plotted is $E_{uu}(k_c)$, the one-dimensional streamwise PSD, as a function of the convective wave number $k_c = \omega / U_c(y)$. These values $E_{uu}(k_c)$ satisfy the property

$$\int_0^\infty E_{uu}(k_c)\, dk_c = \overline{u^2}(y) \qquad (1)$$

At $y$ = 1.02 cm, Fig. 7(a), the MVGs are too far away to have much effect on the power spectrum. However, at $y$ = 1.78 cm and $y$ = 1.91 cm, the plots in Figs. 7(b) and 7(c) show a statistically significant difference between the two flow states. Figs. 7(b) and 7(c) are representative of the five locations at $y$ = 1.52, 1.78, 1.91, 2.03, and 2.16 cm. All five spectra are similar in that the amplitudes for the flow with MVGs are reduced at wave numbers below approximately 300 $m^{-1}$ and are increased at higher wave numbers. At $y$ = 2.29 cm and 2.41 cm, the comparative spectra again become closer as the measurement station enters the boundary layer on the nacelle model underside, with the difference being negligible at the highest station $y$ = 2.51 cm, as shown in Fig. 7(d).

The power spectra were post-processed in order to compute $R_{uu}(\tau)$, the time correlation function, at each vertical measuring station. The type of processing used to calculate $R_{uu}(\tau)$ from $E_{uu}(k_c)$ can be found, e.g., in [15]. The velocity time-correlations, for the baseline flow and the flow with MVGs, are plotted in Figs. 8(a) – 8(d), for the same measurement stations that correspond to the PSD plots in Figs. 7(a) – 7(d). Not surprisingly, the velocity time-correlations compare between the two flow states in a similar manner to the PSDs. The difference is most significant at the interior points, but negligible at the uppermost and lowermost points.

If Taylor's hypothesis is assumed, these time correlation functions can be used to determine streamwise integral length scales in the following way. First, a temporal scale is calculated by integrating the correlation function with respect to all time separations $\tau$. Then the streamwise integral length scale $L_{uu}(y)$ is obtained by multiplying the temporal scale by the local mean flow speed:

$$L_{uu}(y) \approx U_c(y) \int_0^\infty R_{uu}(\tau)\, d\tau \qquad (2)$$

For present purposes, the integration in Eq. (2) is performed only for the first positive lobe of the correlation function. The integral length scales, with and without MVGs in the flow, are compared in Fig. 9. Fig. 9 shows that the application of the MVGs has resulted in a decrease or no change in the streamwise integral length scale at eight of the nine measurement locations.

## 4. Acoustic Analysis

The acoustics of an imaginary airfoil placed in a stator-like position beneath the nacelle model are simulated with the use of the flow measurements. An acoustic source is produced by unsteady lift on the airfoil. In the acoustic analysis that follows, the objective is to determine the difference in sound pressure levels that results when MVGs are installed in the baseline flow. Therefore, an absolute sound pressure level is not required for either the baseline flow or the flow with MVGs, but rather a differential sound pressure level between the two flow states.

### 4.1. Airfoil in Turbulence

Consider an airfoil that is placed in a stator-like position beneath the nacelle model with its leading edge coincident with the data measurement plane as in Fig. 10. The chord length *C* of the stator is 8.89 cm and its span 2*b* is the entire passage height of 2.67 cm. For convenience, a new coordinate system is established so that the data plane is located at *x* = 0, as in Fig. 10. The airfoil chord now exists on $0 \le x \le C$ and its span on $-b \le y \le b$. A stator in this location is subject to inflow turbulence as measured in the data plane and discussed in the preceding section. The turbulent flow field gives rise to an unsteady pressure distribution on the surface of the stator and thereby creates a fluctuating lifting force that is well known to produce noise; see e.g., [16] and [17]. Both the acoustic source and the noise produced by this incident turbulence are analyzed in the following sub-sections.

### 4.2. Broadband Surface Pressure Model

In [18], a surface pressure model for an airfoil in homogeneous, isotropic turbulence was formulated by characterizing the velocity field as a linear superposition of periodic gusts that convect at the freestream speed over a flat plate. These gusts are determined by the spectral content of the turbulent velocity component that is normal to the stator surface. In the present case, this normal component is in the direction of the *z*-axis, i.e., the *w* component. Although the boundary-layer turbulence in the present case is not isotropic and is not homogeneous in the direction of the *y*-axis, the stator surface pressure will be modeled similarly to the analysis in [18] and [19], with a modification to account for non-homogeneity in the *y* direction.

The vertical non-homogeneity of the flow will be accounted for by applying strip theory. The stator surface is divided into streamwise strips as illustrated in Fig. 11. Theoretically, the width of a strip is restricted such that the turbulence within a given strip is uncorrelated with that in an adjoining strip. Within each strip, the flow is assumed isotropic with a streamwise turbulence spectrum that is known from measurement, and the analysis in [19] is applied locally, with a final integration along the *y*-axis.

The evaluation of the stator-surface pressure jump is accomplished by first recognizing the incident turbulent fluctuations as a stochastic process. Such a process can be characterized by a truncated series whose coefficients are chosen such that the autocorrelation of the series forms a Fourier transform pair with its power spectrum (see, e.g., [20]). This property is achieved by evaluating the spectral amplitudes of the surface pressure as a function of the two-dimensional PSD of the stator-normal velocity field. If the stator is considered a flat plate, then, as encountered by the stator surface in the plane $z = 0$, the pressure jump across the stator surface can be approximated by

$$\Delta P(x,y,t) \approx 2\pi\rho_0 U_c \sum_{n=-N}^{N} A_n(y)\, e^{i\phi_n}\, g(x;k_n)\, e^{i k_n U_c t} \qquad (3)$$

$$k_n = n\Delta k_c\,, \qquad n = 0, \pm 1, \pm 2, \ldots, \pm N$$

$$\Delta k_c = k_N / N$$

where $\rho_0$ is the ambient density and $g(x;k_c)$ is a transfer function that is derived from thin airfoil theory [21]. The "upper cutoff" wave number $k_N$ is chosen such that the acoustic source amplitude is considered negligible or is out of measurement range for $k_c > k_N$. The phase angles $\{\phi_n\}$ are independent random variables uniformly distributed on $[0, 2\pi]$. The factor of two in Eq. (3) indicates that the pressure is assumed antisymmetric between the two sides of the stator surface.

The surface pressure amplitudes $A_n(y)$ are now discussed. It is argued by Amiet [18] that, within certain limitations, integration over all spanwise wave numbers is not required, because only one spanwise wave number will significantly contribute to the acoustic signal received by an observer in a fixed location. Using a time-domain approach that is analogous to that of Amiet, it was shown in [19] that only the zero spanwise wave number was acoustically relevant for an observer in a spanwise symmetric location. For an observer in the plane $y = 0$, the amplitudes $A_n(y)$ are determined by

$$A_n(y) = [\,\Phi_{ww}(y;k_n,0)\,\Delta k_c\,]^{\frac{1}{2}} \qquad (4)$$

where the local two-dimensional spectrum $\Phi_{ww}(y;k_c,k_y)$ is interpreted as a three-dimensional PSD of $w$, into which all stator-surface-normal wave numbers are integrated:

$$\Phi_{ww}(y;k_c,k_y) = \int_{-\infty}^{\infty} \Phi_{ww}(y;k_c,k_y,k_z)\, dk_z \qquad (5)$$

It remains to determine $\Phi_{ww}(y;k_c,0)$, the zero-th spanwise wave-number component of the two-dimensional transverse velocity spectrum in Eq. (5). Recall that the streamwise spectrum was measured in the present experiment and, therefore, the transverse spectrum must be determined from it.

### 4.3. Transverse Velocity Spectrum

The transverse velocity spectrum $\Phi_{ww}(k_c,0)$ that is required in Eqs. (3) and (4) is not immediately available, and must be determined from the available measurements. There are two steps in this evaluation. First, the one-dimensional transverse velocity PSD, $E_{ww}(k_c)$, is related to the measured streamwise PSD. Then, an expression is derived that relates the one-dimensional transverse spectrum to $\Phi_{ww}(k_c,0)$. Note that, for the present discussion, the *y* dependence in the flow is suppressed, i.e., the stator surface pressure is modeled within a single strip (Fig. 11).

If the turbulence were isotropic, then the one-dimensional transverse spectrum could be directly related to the measured, one-dimensional streamwise spectrum by (see e.g., [22])

$$E_{ww}(k_c) = \frac{1}{2}\left[ E_{uu}(k_c) - k_c \frac{d}{dk_c} E_{uu}(k_c) \right] \qquad (6)$$

It has been previously demonstrated [23] that Eq. (6) will result in significant error for a transverse spectrum in a boundary layer. Therefore, a single acoustic prediction that incorporates Eq. (6) would also contain significant error, particularly in the lower frequencies, where incident turbulence noise dominates. However, because the desired acoustic prediction is a differential, the result will ultimately rely on a difference of PSD's between the two flow states. Therefore, it could be rationalized that the error made by Eq. (6), as applied to both flow states, would cancel in the final calculation of this differential. There is another problem, however, in the use of Eq. (6) directly on the measured PSD, as represented in Figs. 7(a) – 7(d). The application of the derivative operator to non-smooth data gives wildly fluctuating results as $k_c$ becomes large, as shown in Fig. 12. Consideration was given to smoothing either the measured data or the computed transverse spectrum, but this idea was abandoned on the basis that the final acoustic prediction should not be dependent on the characteristics of a given smoothing algorithm, especially in this case, where the amount of smoothing must increase as the wave number increases. Therefore, a different approach is taken that will allow the use of the measured data as is.

In the work of Bradshaw and Ferris [24], measurements were taken for the PSD of all three velocity components, as a function of the streamwise wave number, in a turbulent boundary layer. It was shown that the measured spectra for a given velocity component, at different locations within the boundary layer, would collapse when scaled on inner variables. Fig. 13 shows the collapsed results for the spectral densities of all three velocity components, as interpreted in [25]; see Fig. 5-38 in that reference. The values plotted in Fig. 13 are the one-dimensional streamwise and transverse power spectra, scaled by $\rho_0 U_c/\tau_w y$, where $\tau_w$ is the wall shear stress. The spectra are given as functions of the dimensionless quantity $\omega y/U_c$. Recall that $U_c$ is a function of *y*.

An ad hoc function $h(k_c)$ is now desired that will provide a scaling relationship between the streamwise and transverse spectra, i.e.

$$E_{ww}(k_c) \approx h(k_c)\, E_{uu}(k_c) \qquad (7)$$

Fig. 14 shows an example of the application of the inner-variable scaling in Fig. 13 for the present case, using specific values of $y$ = 1.78 cm and $U_c$ = 31.91 m/sec, which correspond to one of the present measurement stations. The scaled spectra in Fig. 14 are plotted as a function of $k_c$. The darkened symbols in Fig. 14 represent the values of the streamwise spectrum, having been scaled by a function $h(k_c)$ of the form

$$h(k_c) = 1 - \alpha_y \log_{10}(k_{\max}/k_c)\ , \qquad 0 < k_c < k_{\max} \qquad (8)$$

where $k_{\max}$ is chosen so that $f_{\max} = 10$ kHz and $\alpha_y = 0.270$ for the case in Fig. 14. Note the close agreement between the product $h(k_c)E_{uu}$ and the inner-variable-scaled transverse spectrum, i.e. Eq. (7) is satisfied. It was found that, when using all current measurement stations on $1.02\,\text{cm} \le y \le 2.51\,\text{cm}$, with corresponding convection speeds $U_c(y)$ from Fig. 5, similar plots to Fig. 14 were generated and found to satisfy the relationship in Eqs. (7) and (8). The values of the parameter $\alpha_y$ were required to range from 0.255 to 0.290 in order to establish a specific scaling function $h(k_c)$ for each measurement station. The values of $\alpha_y$ for all nine stations are shown in Table I. Note that $\alpha_y$ is nearly constant with values ranging from 0.268 to 0.275 on $1.52\,\text{cm} \le y \le 2.16\,\text{cm}$. The measured difference between the baseline spectra and the spectra with MVGs was most significant within this vertical span of the data measurement plane (See Figs. 7(b) and 7(c).).

Although this approach is ad hoc, again, the rationale is that the error made in this approximation will cancel in the final differential calculation, provided that $h(k_c)$ is a relatively weak function in *y,* as is

suggested by the relatively uniform values of $\alpha_y$ on the inner measurement stations where the spectra were most affected by the MVGs. Furthermore, the measured data for $E_{uu}(k_c)$ can be used as is, without concern for pre- or post-processing. As an example application to current data, Fig. 15 shows the computed values of $E_{ww}(k_c)$, using the measured streamwise spectrum $E_{uu}(k_c)$ at $y$ = 1.78 cm and the scaling law in Eqs. (7) and (8). In order to provide a sanity check for the scaling method in Eqs. (7) and (8), the computed values of the baseline transverse spectra are integrated to calculate a transverse mean-square turbulence, i.e.,

$$\int_0^\infty E_{ww}(k_c)\, dk_c = \overline{w^2}(y) \tag{9}$$

The values in Eq. (9) are used to determine a transverse turbulence intensity $w_{\text{rms}}/U_\infty$ at each vertical measurement station, as shown in Table I. The ratios of streamwise and transverse turbulence intensities are reasonably consistent with the turbulence intensity data of Klebanov [23] in the boundary layer region $0.22 \le y/\delta \le 0.53$ (See Figure 4 in [23].). The computed vales in Table I are not expected to be identical to the data in [23], as the present experiment does not deal with a simple flat plate boundary layer, but one that contains an obstruction.

The one-dimensional transverse PSD, $E_{ww}(k_c)$, must now be related to $\Phi_{ww}(k_c,0)$, the PSD that is required to model the stator surface pressure in Eqs. (3) and (4). This can be accomplished as argued by Amiet in [18]. Amiet's argument relies on the assumption of isotropy, which is interpreted in the present context as "isotropic within a strip." First, consider the quantity $R_{ww}(k_c,\eta)$, a cross-PSD of the transverse velocity fluctuations, whose values are correlated through a stator-spanwise distance $\eta$, i.e.

$$R_{ww}(k_c,\eta) = \int_{-\infty}^{\infty} \Phi_{ww}(k_c,k_y)\, e^{ik_y\eta}\, dk_y \tag{10}$$

If $R_{ww}(k_c,\eta)$ is integrated in $\eta$, then the result is proportional to a spanwise correlation length. In fact, a stator-spanwise correlation length $\ell_y(\omega)$ can be defined

$$\begin{aligned} \ell_y(\omega) &= \frac{1}{R_{ww}(k_c,0)} \int_0^\infty R_{ww}(k_c,\eta)\, d\eta \\ &= \frac{\pi}{R_{ww}(k_c,0)}\, \Phi_{ww}(k_c,0) \end{aligned} \tag{11}$$

The second equality in Eq. (11) follows from the Fourier transform relation between $R_{ww}$ and $\Phi_{ww}$ [18].

Now, the autocorrelation $R_{ww}(k_c,0)$ in Eq. (11) is the equivalent of $E_{ww}(k_c)$ because it represents a one-dimensional PSD in wave number space. This is readily apparent by setting $\eta = 0$ in Eq. (10):

$$R_{ww}(k_c,0) = \int_{-\infty}^{\infty} \Phi_{ww}(k_c,k_y)\, dk_y \equiv E_{ww}(k_c) \tag{12}$$

Eqs. (11) and (12) relate the one-dimensional transverse PSD to the spectrum $\Phi_{ww}(k_c,0)$ that is required in the stator surface pressure model. Finally, using Eq. (7), $\Phi_{ww}(k_c,0)$ is related to the measured streamwise PSD by

$$\Phi_{ww}(k_c,0) = \frac{1}{\pi}\, \ell_y(\omega)\, h(k_c)\, E_{uu}(k_c) \tag{13}$$

where $h(k_c)$ is given by Eq. (8). If the flow is assumed isotropic within a strip, then the correlation length $\ell_y(\omega)$ can be calculated by

$$\ell_y(\omega) = \frac{8L_{uu}}{3}\left[\frac{\Gamma(1/3)}{\Gamma(5/6)}\right]^2 \frac{(k_c/k_E)^2}{[3+8(k_c/k_E)^2][1+(k_c/k_E)^2]^{1/2}} \tag{14}$$

where $\Gamma(\cdot)$ denotes the well-known Gamma function (see, e.g., [26]), and $k_E$ is the peak wave number and is approximately $k_E \approx 0.747/L_{uu}$. See [18] for a derivation of Eq. (14).

Eq. (13) is an important result. Whenever possible, it is desirable to use a streamwise, one-dimensional spectrum because the quantity $E_{uu}(k_c)$ is typically the simplest spectrum to measure in a turbulent flow, and can be accomplished with a single hot-wire element. Eqs. (13) and (14) now enable the evaluation of the stator surface pressure in Eq. (3). Such approximations as discussed above for the modeling of surface pressure in non-homogeneous, anisotropic turbulence are admittedly crude. However, the formulation for the desired differential in sound pressure levels will ultimately rely on the ratio of two acoustic powers in which significant cancellation occurs, as discussed in Section 4.5.

### 4.4 Acoustic Formulation

The desired noise level comparison will be accomplished with an acoustic formulation introduced in [27]. This time-domain formulation, called "Formulation 1A," is a solution of the Ffowcs Williams-Hawkings equation [28]. For the present case, the observer location $\vec{x}$ will be assumed to be at a distance $r$ directly outward from the geometric center of the

stator surface, i.e., in the plane $y = 0$. Furthermore, the Mach number of the mean flow is small ($M \approx 0.1$) and the observer location is presumed in the acoustic far field, as well as the geometric far field, i.e, the following conditions are satisfied:

$$M \ll 1, \qquad r \gg \lambda, \qquad r \gg C \tag{15}$$

where $\lambda = c_0 / f$ is the largest acoustic wavelength of interest, and $c_0$ is the sound speed. Under such conditions, Formulation 1A allows the acoustic pressure $p'(\vec{x},t)$ received by the observer to be approximated by a simple surface pressure integration, which can be written

$$4\pi\, p'(\vec{x},t) \approx \frac{1}{c_0\, \bar{r}} \int_{-b}^{b} \int_{0}^{C} \frac{\partial}{\partial \tau}\, p(\bar{\tau})\; dx\, dy \tag{16}$$

where $\bar{r}$ is the mean observer distance to the stator surface, and $p(\bar{\tau})$ is the pressure on the stator surface evaluated at a mean retarded time, i.e.,

$$p(\bar{\tau}) = \Delta P(x, y, \bar{\tau}), \qquad \bar{\tau} = t - \bar{r} / c_0 \tag{17}$$

If the surface pressure jump in Eq. (3) is substituted in Eqs. (16) and (17), the result is the following expression for the acoustic pressure signal at the observer in the far field:

$$p'(\vec{x},t) \approx \tag{18}$$
$$\int_{-b}^{b} \int_{0}^{C} \frac{\rho_0 U_c^2}{2 c_0 \bar{r}} \sum_{n=-N}^{N} A_n(y)\, i k_n\, g(x;k_n)\; e^{i(k_n U_c \bar{\tau} + \phi_n)} dx\, dy$$

For convenience, the acoustic signal in Eq. (18) is rewritten as

$$p'(\vec{x},t) \;\approx\; \frac{\rho_0}{2 c_0 \bar{r}} \int_{-b}^{b} \sum_{n=-N}^{N} i U_c^2 k_n\, I_n\; A_n(y)\, e^{i(k_n U_c \bar{\tau} + \phi_n)}\; dy \tag{19}$$

where

$$I_n = \int_0^C g(x;k_n)\, dx \tag{20}$$

A formula for the integral in Eq. (20) is given in [21]; see Equations 18 and 19 of that reference.

### 4.5 Incident Turbulence Noise Comparison

Baseline noise levels and noise levels that include the effect of MVGs are now compared. These noise levels are based on acoustic pressure signals as evaluated by Eq. (19). The numerical evaluation of the spanwise integral in Eq. (19) requires a discretization of the stator span according to the nine flow measurement locations $\{y_j\}_{j=1}^{9}$. To this end, the far field noise associated with the unsteady surface pressure on the j-th strip is denoted $p'_j(\vec{x},t)$, and is defined by

$$p'(\vec{x},t) \approx$$
$$\sum_{j=1}^{9} \sum_{n=-N}^{N} \frac{\rho_0}{2 c_0 \bar{r}}\, i\, U_c^2\, k_n\, I_n\; A_n(y_j)\, e^{i(k_n U_c \bar{\tau} + \phi_n)}\; \Delta_j$$
$$\equiv \sum_{j=1}^{9} p'_j(\vec{x},t) \tag{21}$$

where $\Delta_j$ is the discrete stator-spanwise spacing determined by the flow measurement locations.

The quantity to be compared is the sound pressure level (SPL). The SPL associated with the acoustic source on the j-th strip is defined by

$$SPL_j(f_n) = 10 \log \left\{ \frac{\overline{P_{n,j}^2}}{P_{\text{ref}}^2} \right\} \tag{22}$$

where $\overline{P_{n,j}^2}$ is the acoustic PSD due to the source on the j-th strip at the frequency $f_n$. The over-bar denotes a time average, and $P_{\text{ref}}$ is a reference pressure most commonly taken to be 20 μPa. The values of the pressure spectrum $\{P_{n,j}\}$ are the resulting amplitudes of a Fourier analysis of the time series in Eq. (21) at a point $y_j$ on $-b < y_j < b$. The total SPL is obtained by power-summing the contributions due to the component sources on each strip:

$$SPL(f_n) = 10 \log \left\{ \sum_{j=1}^{9} 10^{\;0.1\, SPL_j(f_n)} \right\} \tag{23}$$

The far field acoustic pressure due to the source on the j-th strip in Eq. (21) can be written in the form

$$p'_j(t) \;=\; \sum_{n=-N}^{N} \hat{q}_{n,j}\; e^{i \omega_{n,j} t} \tag{24}$$

where $\omega_n = k_n U_c$. It can be shown (see, e.g., [29]) that the time average of $[p'_j(t)]^2$ can be evaluated as

$$\overline{[p'_j(t)]^2} = \overline{[p'_j(t)][p'_j(t)]^*} = \sum_{n=-N}^{N} \left| \hat{q}_{n,j} \right|^2 = \sum_{n=0}^{N} \overline{P_{n,j}^2} \tag{25}$$

where the star superscript a denotes complex conjugate. Eqs. (22), (23), and (25) allow the total SPL at a given non-negative frequency to be written

$$SPL(f_n) = 10 \log\left\{ \frac{2}{P_{\text{ref}}^2} \sum_{j=1}^{9} \left|\hat{q}_{n,j}\right|^2 \right\} \tag{26}$$

and

$$\begin{aligned} \left|\hat{q}_{n,j}\right|^2 &= \hat{q}_{n,j}\ \hat{q}^*_{n,j} \\ &= \frac{\rho_0^2}{4\, c_o^2\, \bar{r}^2} \left[ U_c^4 \left|I_n\right|^2 k_n^2\, A_n^2 \right]_j \Delta_j^2 \end{aligned} \tag{27}$$

Note that the surface pressure amplitudes $\{A_n\}$ are real. In order to compare noise levels arising from the two flow states, let the subscript notation $(\cdot)_B$ and $(\cdot)_V$ represent quantities that are evaluated with respect to the baseline flow and the flow with MVGs, respectively. Using Eqs. (26) and (27), the desired SPL differential induced by the entire stator source is evaluated by

$$\begin{aligned} \Delta SPL(f_n) &\equiv \left[SPL(f_n)\right]_V - \left[SPL(f_n)\right]_B \\ &= 10 \log\left\{ \frac{\displaystyle\sum_{j=1}^{9} \left\{ \left[ U_c^4 \left|I_n\right|^2 k_n^2\, A_n^2 \right]_j \right\}_V \Delta_j^2}{\displaystyle\sum_{j=1}^{9} \left\{ \left[ U_c^4 \left|I_n\right|^2 k_n^2\, A_n^2 \right]_j \right\}_B \Delta_j^2} \right\} \end{aligned} \tag{28}$$

where $A_n$ is given in Eqs. (4), (13), and (14).

Fig. 16 is a plot of Eq. (28), using the current measurements at the nine stations along $z$ = 0, as a function of frequency. The application of the MVGs has resulted in an SPL differential in the overall range of approximately ±2 dB out to 27 kHz. Note the average relative decrease in SPL below approximately two kHz.

For present purposes, Eq. (28) can be further simplified by the following reasoning. First, the value of $I_n$ is relatively insensitive to the convection speed for low Mach number flows [21], and therefore is nearly constant throughout the data measurement plane, for a given frequency. The ad hoc scaling function $h(k_c)$ that occurs Eq. (13) is also nearly constant in $y$ for a fixed frequency, in particular for those locations at which the MVGs have their largest impact on the turbulence spectrum. Furthermore, the stator-spanwise correlation length $\ell_y(\omega)$ is virtually independent of $y$ for all but the lowest wave numbers as can be seen by the following proportionality when $k_c >> 1$ in Eq. (14):

$$\ell_y(\omega) \propto \frac{L_{uu}\,(k_c/k_E)^2}{(k_c/k_E)^2 (k_c/k_E)} \propto \frac{1}{k_c} \tag{29}$$

Recall that $k_E \propto 1/L_{uu}$. Now, if Eqs. (4), (13), and (14) are substituted for $A_n^2$ in Eq. (28) and $I_n$, $h(k_c)$, and $\ell_y(\omega)$ are nearly constant in $y$ for a fixed frequency, then some algebraic manipulation yields the following simplification of Eq. (28):

$$\Delta SPL(f_n) \;=\; 10 \log\left\{ \frac{\displaystyle\sum_{j=1}^{9} \left\{ \left[U_c\, E_{uu}(k_n)\right]_j \right\}_V \Delta_j^2}{\displaystyle\sum_{j=1}^{9} \left\{ \left[U_c\, E_{uu}(k_n)\right]_j \right\}_B \Delta_j^2} \right\} \tag{30}$$

Note the significant simplification in Eq. (30) that occurs as a result of cancellation, owing to the differential formulation. The SPL differential, as predicted by Eq. (30) with the measured input, is shown in Fig. 17. The plot in Fig. 17 is visually indistinguishable from Fig. 16, thereby requiring separate figures for their comparison.

As a final calculation, upper and lower bounds of the SPL differential are established by using data from a measurement station in which the difference in turbulence spectra is most prominent, say at $y$ = 1.91 cm. Fig. 18 shows an SPL differential as predicted with the assumption that the mean flow and turbulence spectrum as measured at $y$ = 1.91 cm is held constant throughout the vertical extent of the measurement plane. Under this "worst case" scenario, the SPL differential range has been extended from approximately –3 dB to 5 dB. The reasoning behind such a calculation is to help determine if an economical procedure can be developed for flow control design studies, i.e., when only one measurement is affordable for each point in a design matrix.

## 5. Concluding Remarks

Micro vortex generators (MVGs) have been tested in a wind tunnel to quantitatively assess their effect on the velocity field within the wake region of a turbulent boundary layer. Measurements of the mean flow and turbulence indicated that the MVGs had a measurable effect on the flow, relative to the baseline. Velocity power spectra and integral length scales of the turbulence were altered at a vertical distance several times the height of the MVGs. The application of the MVGs resulted in a reduction in power spectral amplitude at frequencies below approximately 1500 Hz, and an increase at higher frequencies. In addition, the streamwise integral length scales were reduced by as much as 14 percent. A decrease in streamwise length scales suggests that the MVGs have reorganized the turbulence in a more isotropic fashion, although

additional measurements would be necessary to confirm this.

The potential acoustic impact of the MVGs was analyzed. The acoustic analysis resulted in a relatively simple formulation that was used to determine the additional noise that such devices impart to a turbulent flow. Measured turbulence spectra were input to the acoustic formulation to predict the effect of the MVGs on radiated noise that results from incident turbulence. The acoustic analysis indicated that the MVGs would cause a relatively small change in sound pressure levels of approximately ±2 dB. Acoustic measurements would be required to fully validate this analytical approach.

## References


1. Taylor, H. D., "The Elimination of Diffuser Separation by Vortex Generators," *United Aircraft Corporation Report No. R-4012-3*, June 1947.
2. Schubauer, G. B., and Spangenber, W. G., "Forced Mixing in Boundary Layers," *Journal of Fluid Mechanics*, Vol. 8, Part 1, 1960, pp. 10 –32.
3. Pearcey, H. H., "Shock Induced Separation and Its Prevention by Design and Boundary-Layer Control," Boundary Layer and Flow Control, Vol. 2, ed. G. V. Lachman, Pergamon Press, New York, 1961, pp. 1166 –1344.
4. Shaw, R. J., "An Experimental Investigation of Force Mixing of A Turbulent Boundary Layer in an Annular Diffuser," *NASA TM 79171*, April 1979.
5. Lin, J. C., Howard, F. G., and Selby, G. V., "Small Submerged Vortex Generators for Turbulent Flow Separation Control," *Journal of Spacecraft and Rockets*, Vol. 27, No. 5, Sept.-Oct. 1990, pp. 503 – 507.
6. Lin, J. C., "Control of Turbulent Boundary-Layer Separation Using Micro-Vortex Generators," *AIAA Paper 99-3404*, 30th AIAA Fluid Dynamics Conference, Norfolk, VA, June 28-July 1, 1999.
7. Lin, J. C., Robinson, S. K., McGhee, R. J., and Valarezo, W. O., "Separation Control on High-Lift Airfoils Via Micro-Vortex Generators," *Journal of Aircraft*, Vol. 31, No. 6, Nov.-Dec. 1994, pp. 1317 –1323.
8. Jenkins, L., Gorton, S. A., and Anders, S., "Flow Control Device Evaluation for An Internal Flow with An Adverse Pressure Gradient," *AIAA Paper 2002-0266*, 40th AIAA Aerospace Sciences Meeting and Exhibit, Reno, NV, January 14-17, 2002.
9. Hamstra, J. W., Miller, D. N., Truax, P. P., Anderson, B. H., and Wendt, B. J., "Active Inlet Flow Control Technology Demonstration," ICAS-2000-6.11.2, 22nd International Congress of the Aeronautical Sciences, Aug.-Sept. 2000.
10. Anderson, B. H. and Gibb, J., "Vortex-Generator Installation Studies on Steady-State and Dynamic Distortion," *AIAA Journal of Aircraft*, Vol. 35, No. 4, 1998, pp. 513 – 520.
11. Anderson, B. H., Miller, D. N., Yagle, P. J., and Truax, P. P., "A Study on MEMS Flow Control for the Management of Engine Face Distortion in Compact Inlet Systems," ASME Paper FEDSM99-9620, *Proceedings of the 3rd ASME/JSME Joint Fluids Engineering Conference*, July 1999.
12. Sullerey, R. K., Mishra, S., and Pradeep, A. M., "Application of Boundary Layer Fences and Vortex Generators in Improving Performance of S-Duct Diffusers," *Journal of Fluids Engineering*, Vol. 124, 2002, pp. 136 –142.
13. Sandborn, V. A., Resistance Temperature Transducers, Metrology Press, Fort Collins, 1972.
14. Pack, L. G., and Seifert, A., "Multiple Mode Actuation of a Turbulent Jet," *AIAA Paper 01-0735*, 39th AIAA Aerospace Sciences Meeting and Exhibit, Reno, NV, January 8-11, 2001.
15. Bendat, J. S. and Piersol, A. G., Random Data: Analysis and Measurement Procedure, second edition, John Wiley and Sons, New York, 1986.
16. Lamb, H., Hydrodynamics, New York, Dover Publications, 6th edition, 1932, p. 501.
17. Curle, N., "The Influence of Solid Boundaries upon Aerodynamics Sound," *Proceedings of the Royal Society A231*, 1954, pp. 505 – 514.
18. Amiet, R. K., "Acoustic Radiation from an Airfoil in a Turbulent Stream," *Journal of Sound and Vibration*, Vol. 41, 1975, pp. 407 – 420.
19. Casper, J. and Farassat, F., "A New Time Domain Formulation for Broadband Noise Predictions," *International Journal of Aeroacoustics*, Vol. 1, No. 3, 2002, pp. 207 – 240.
20. Shinozuka, M. and Deodatis, G., "Simulation of Stochastic Processes by Spectral Representation," *Applied Mechanics Review*, Vol. 44, No. 4, 1991, pp. 191 – 204.
21. Amiet, R. K., "High Frequency Thin-Airfoil Theory for Subsonic Flow," *AIAA Journal*, Vol. 14, No. 8, 1976, pp. 1076-1082.

22. Hinze, J. O., Turbulence, second edition, McGraw-Hill, 1975.

23. Klebanov, P. S., "Characteristics of Turbulence in a Boundary Layer with Zero Pressure Gradient," *NACA Report 1247*, 1955.

24. Bradshaw, P. and Ferriss, D. H., "The Response of a Retarded Equilibrium Turbulent Boundary Layer to the Sudden Removal of Pressure Gradient," *National Physics Lab Aero Report 1145*, 1965.

25. White, F. M., Viscous Fluid Flow, McGraw-Hill, 1974.

26. Abramowitz, M. and Stegun, I. A., Handbook of Mathematical Functions, Dover, 1972.

27. Farassat, F. and Succi, G. P., "The Prediction of Helicopter Rotor Discrete Frequency Noise," *Vertica*, Vol. 7, No. 4, 1983, pp. 309 – 320.

28. Ffowcs Williams, J. E. and Hawkings, D. L., "Sound Generation by Turbulence and Surfaces in Arbitrary Motion," *Philosophical Transactions of the Royal Society*, A 264, 1969, pp. 321 – 342.

29. Pierce, A. D., Acoustics, Acoustical Society of America, New York, 1991.

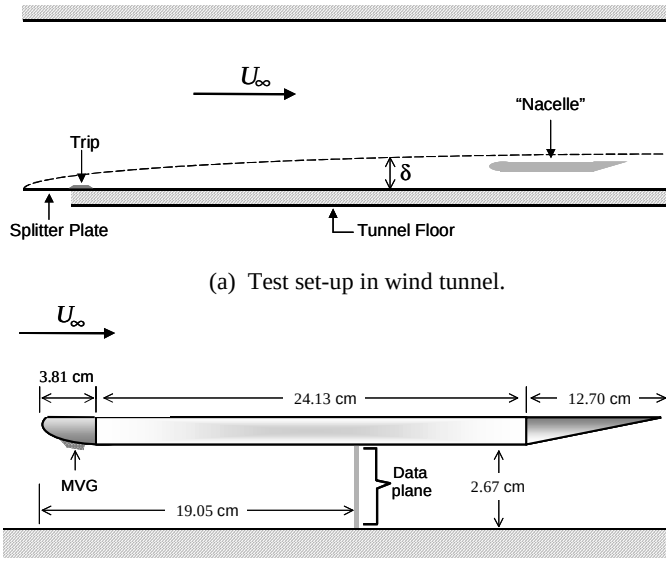


(a) Test set-up in wind tunnel.

(b) ''Nacelle'' model dimension.

**Figure 1.** Schematics for experimental set-up.

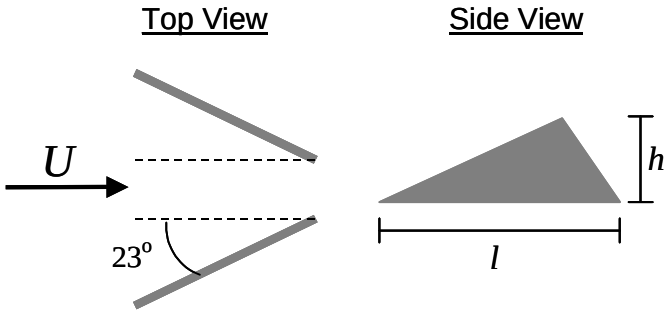


**Figure 2.** Delta-wing MVG geometry.

| $y$ (cm) | $U_c$ (m/s) | $\alpha_y$ | $u_{rms}/U_\infty$ (%) | $w_{rms}/U_\infty$ (%) | $w_{rms}/u_{rms}$ |
|---|---|---|---|---|---|
| 1.02 | 29.76 | 0.290 | 5.86 | 4.23 | 0.72 |
| 1.52 | 31.17 | 0.275 | 5.32 | 3.93 | 0.74 |
| 1.78 | 31.91 | 0.270 | 5.08 | 3.79 | 0.75 |
| 1.91 | 32.25 | 0.270 | 4.86 | 3.66 | 0.75 |
| 2.03 | 32.50 | 0.270 | 4.72 | 3.54 | 0.75 |
| 2.16 | 32.69 | 0.268 | 4.67 | 3.52 | 0.76 |
| 2.29 | 32.29 | 0.265 | 4.84 | 3.73 | 0.77 |
| 2.41 | 30.21 | 0.260 | 5.88 | 4.70 | 0.80 |
| 2.51 | 26.66 | 0.255 | 6.51 | 5.37 | 0.83 |

**Table I.** Scaling values and turbulence intensities for baseline flow state.

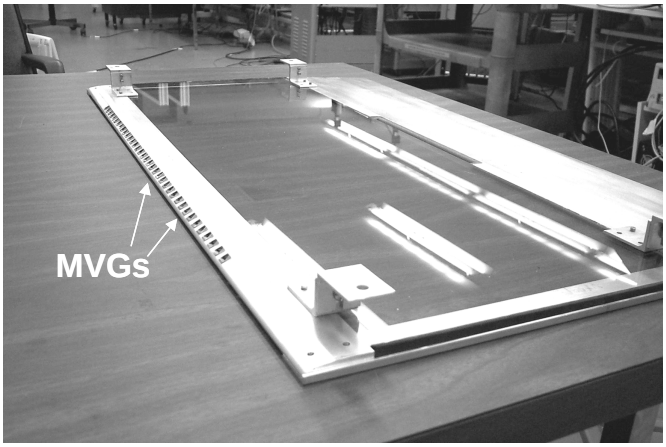


**Figure 3.** Underside view of nacelle model with MVGs.

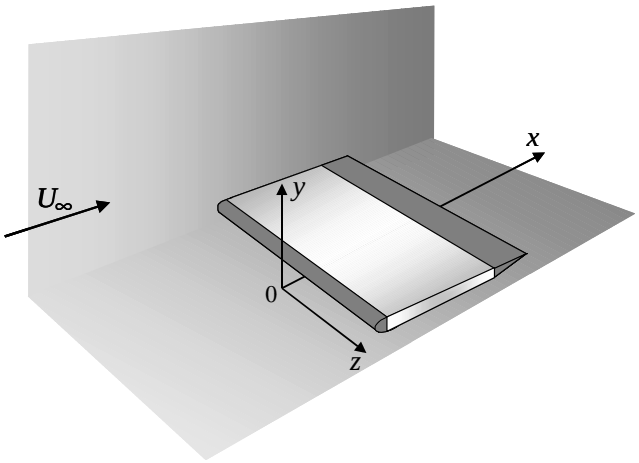


**Figure 4.** Experimental coordinate system.

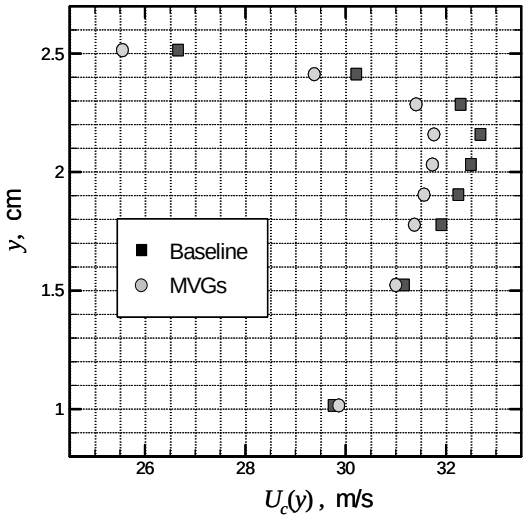


**Figure 5.** Mean flow at $z = 0$.

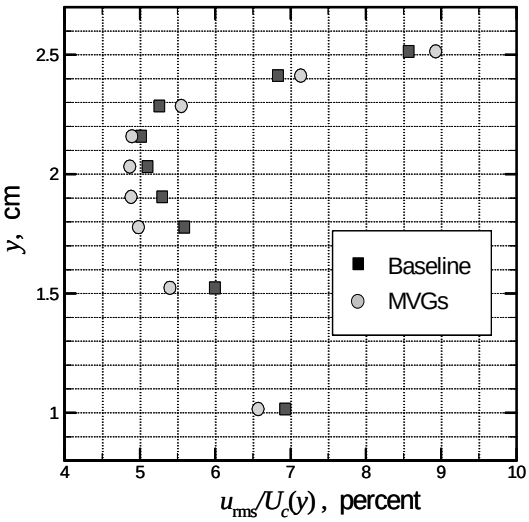


**Figure 6.** Local turbulence intensity at $z = 0$.

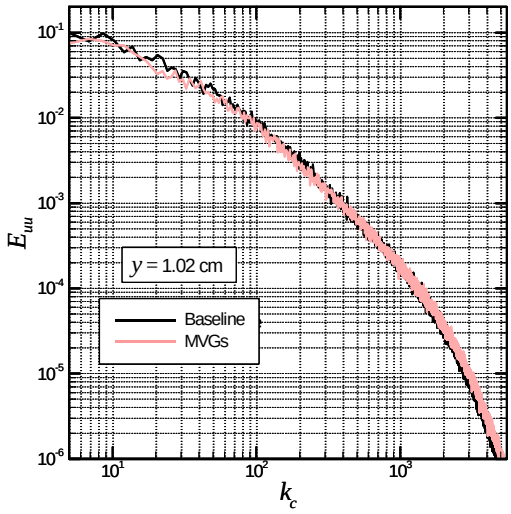


**Figure 7(a).** Turbulence power spectra at $y = 1.02$ cm.

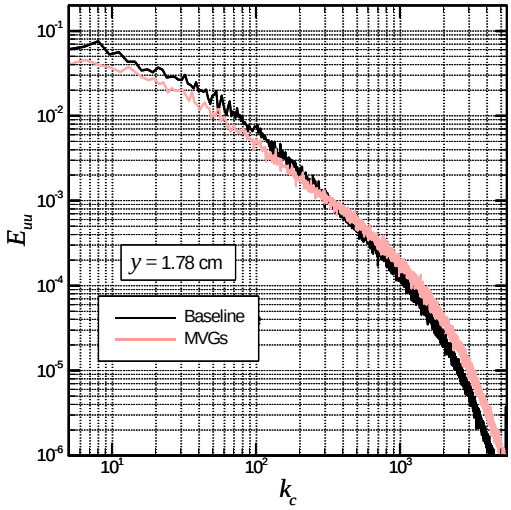


**Figure 7(b).** Turbulence power spectra at $y = 1.78$ cm.

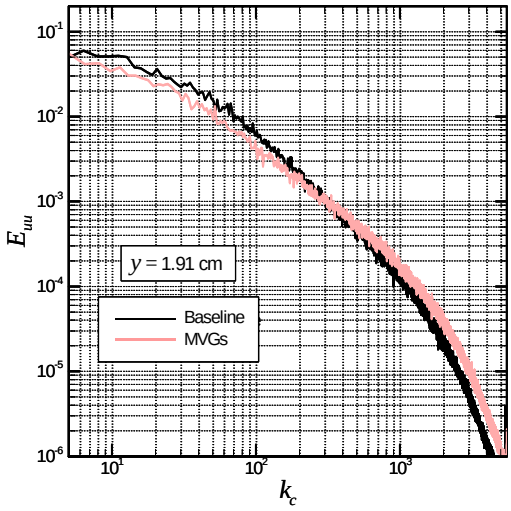


**Figure 7(c).** Turbulence power spectra at $y = 1.91$ cm.

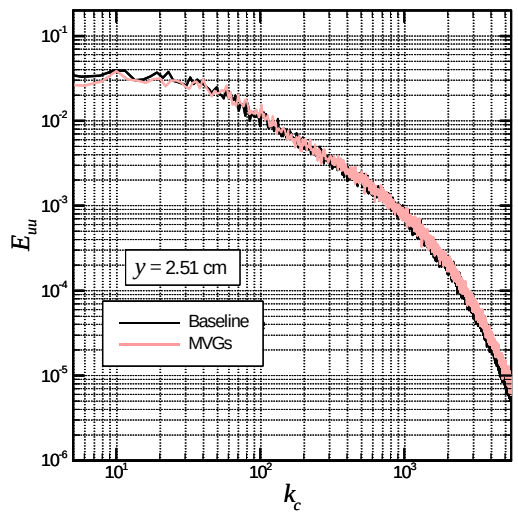


**Figure 7(d).** Turbulence power spectra at $y$ = 2.51 cm

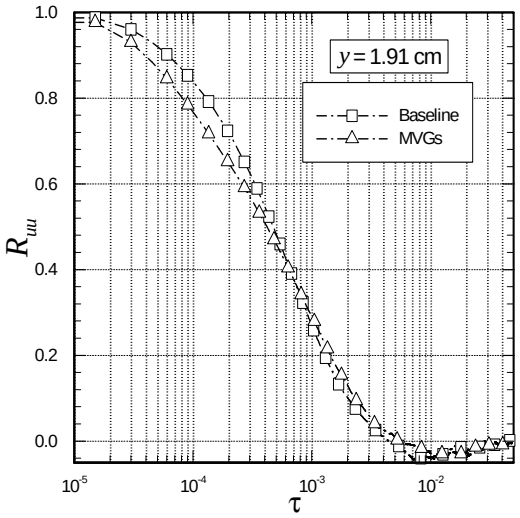


**Figure 8(c).** Velocity time correlations at $y$ = 1.91 cm.

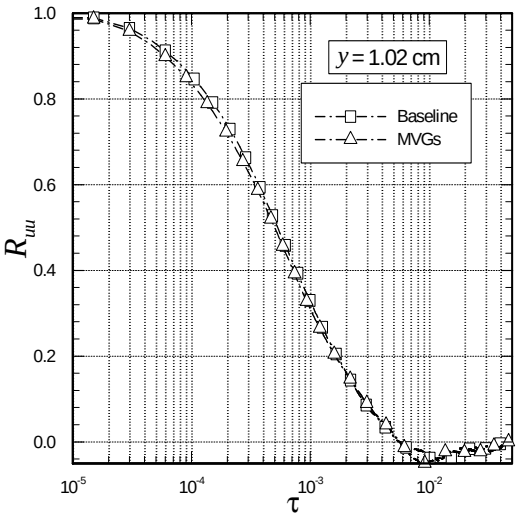


**Figure 8(a).** Velocity time correlations at $y$ = 1.02 cm.

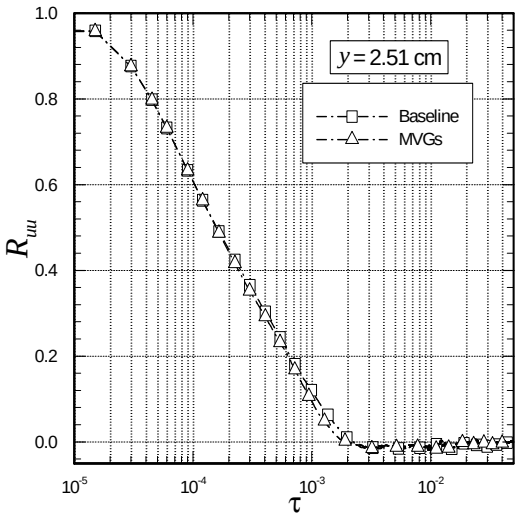


**Figure 8(d).** Velocity time correlations at $y$ = 2.51 cm.

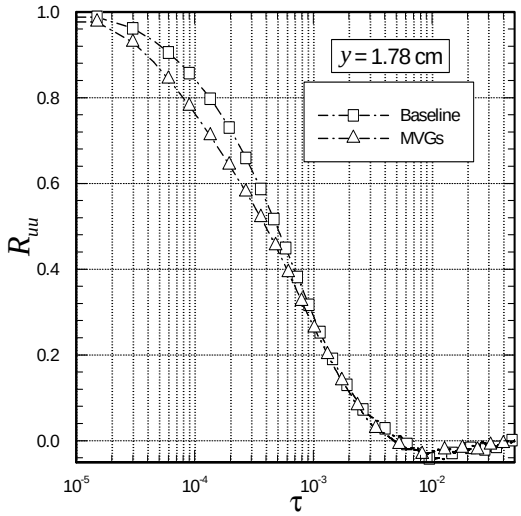


**Figure 8(b).** Velocity time correlations at $y$ = 1.78

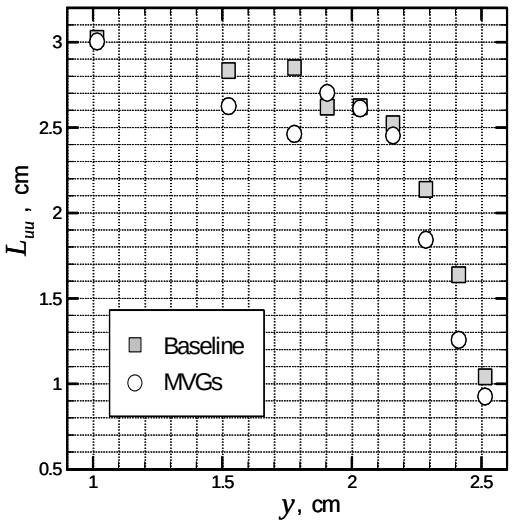


**Figure 9.** Streamwise integral length scales.

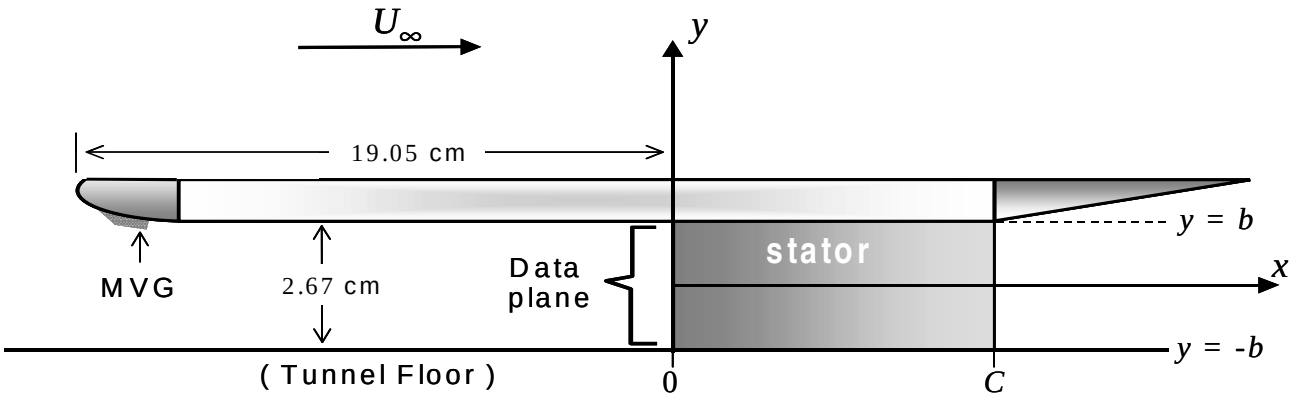


**Figure 10.** Placement of imaginary stator with leading edge at data measurement plane. Coordinate origin moved to stator leading edge for acoustic analysis.

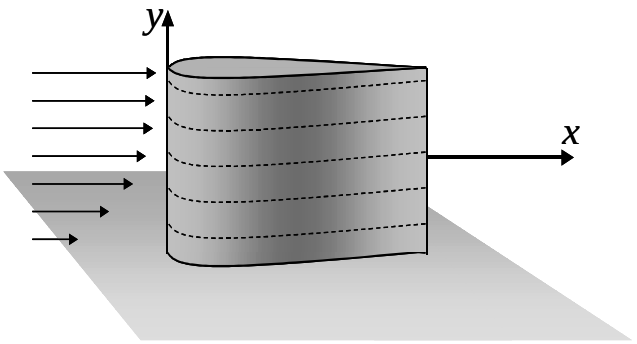


**Figure 11.** Strip theory schematic for sstator surface pressure. Isotropy within a strip is assumed in the analysis.

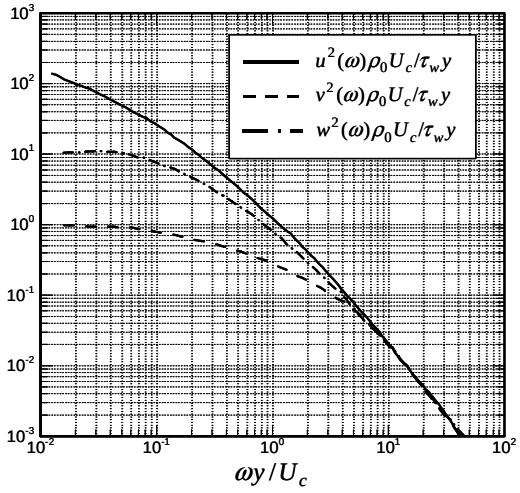


**Figure 13.** Streamwise, wall-normal, and transverse velocity spectra, scaled on inner variables. Data of Bradshaw and Ferriss [24], as interpreted by White [25].

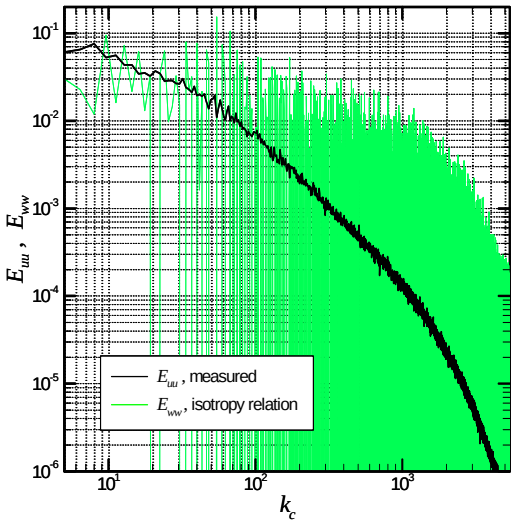


**Figure 12.** Streamwise spectrum as measured at $y$ = 1.02 cm, and transverse spectrum as computed by the isotropic relation in Eq. (6).

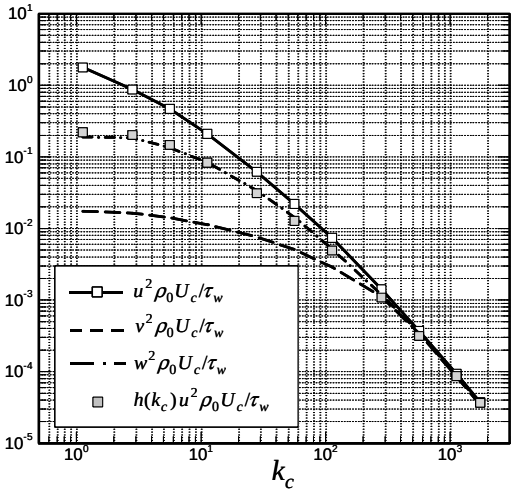


**Figure 14.** Scaled spectra from Fig. 13 with $y$ = 1.78 cm and $U_c = 31.91$ m/s. Dark symbols are the streamwise spectrum scaled by $h(k_c)$ in Eq. (8) with $\alpha_y = 0.270$.

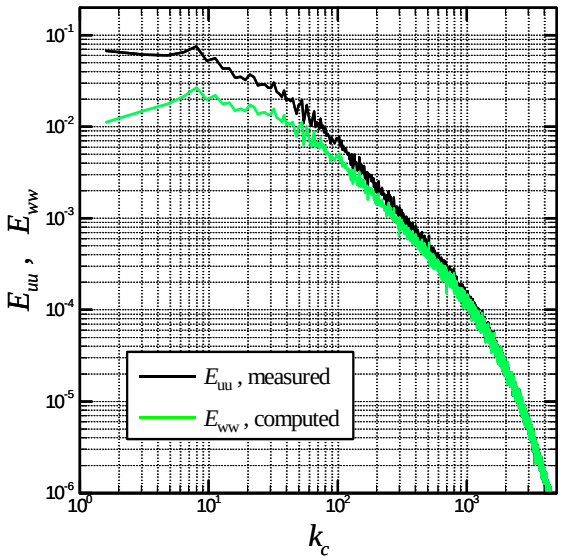


**Figure 15.** Measured streamwise PSD , at $y$ = 1.78 cm; transverse PSD computed with scaling laws in Eqs. (7) and (8), and $\alpha_y = 0.270$ .

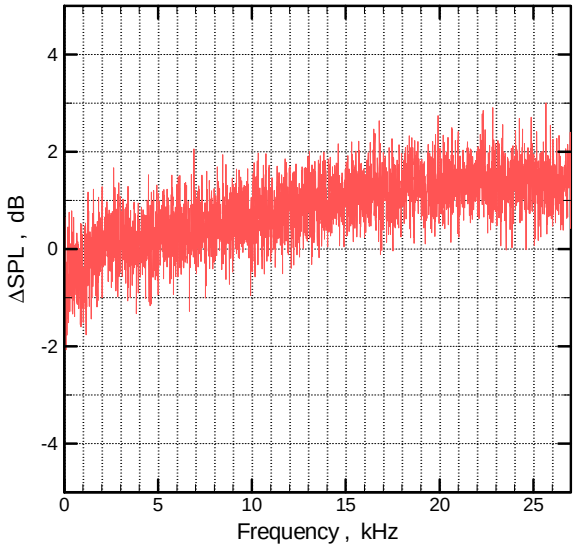


**Figure 17.** Difference in SPLs between the baseline flow and the flow with MVGs, as predicted by Eq. (30) with experimental input.

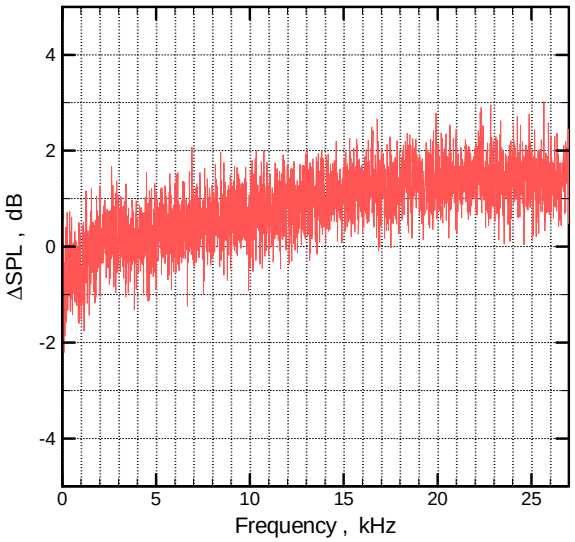


**Figure 16.** Difference in SPLs between the baseline flow and the flow with MVGs, as predicted by Eq. (28) with experimental input.

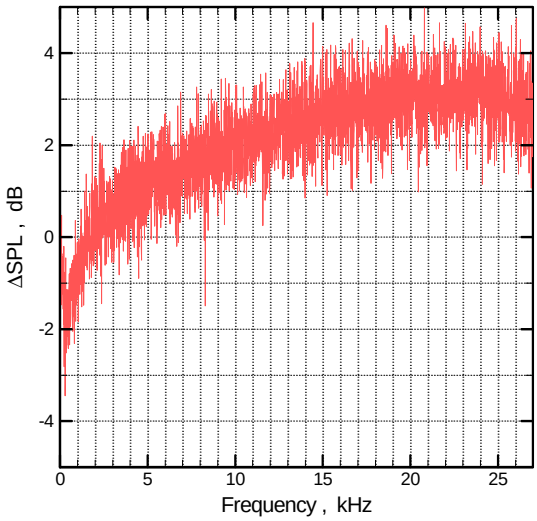


**Figure 18.** "Worst case" SPL differential, as predicted by Eq. (30) with experimental input only from measurement station $y$ = 1.91 cm.